TABLE OF CONTENTS (TOC)

Hybrids of gold nanoparticles and oligo(*p*-phenyleneethynylene)s end-functionalized with alkynylruthenium groups: outstanding two-photon absorption in the second biological window

Cristóbal Quintana, Mahbod Morshedi, Jun Du, Joseph P.L. Morrall, Jan K. Zaręba, Marek Samoc, Marie P. Cifuentes and Mark G. Humphrey*

Australian National University, Australia, and Wroclaw University of Science and Technology, Poland

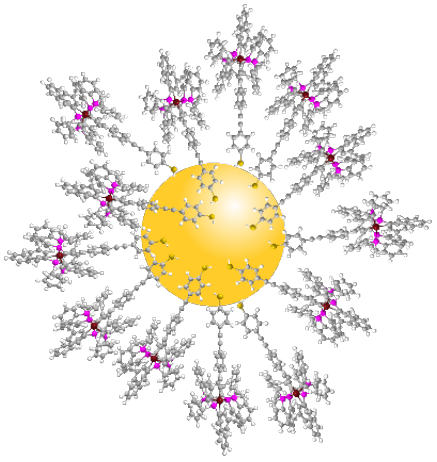

Oligo(*p*-phenyleneethynylene)s (OPEs) end-capped with (alkynyl)bis(diphosphine)ruthenium and thiol/thiolate groups stabilize ca. 2 nm diameter gold nanoparticles (AuNPs) affording OPE/AuNP hybrids that display long-term stability in solution (more than a month), good solubility in organic solvents, reversible ruthenium-centered oxidation, and transparency beyond 800 nm, and possess very strong nonlinear absorption activity at the first biological window, and unprecedented two-photon absorption activity in the second biological window (σ_2 up to 38,000 GM at 1050 nm).

Nano Research

ISSN 1998-0124 CN 11-5974/O4
https://doi.org/(automatically inserted by the publisher)

Hybrids of gold nanoparticles and oligo(*p*-phenyleneethynylene)s end-functionalized with alkynylruthenium groups: outstanding two-photon absorption in the second biological window

Cristóbal Quintana[1], Mahbod Morshedi[1], Jun Du[1], Joseph P.L. Morrall[1], Jan K. Zaręba[2], Marek Samoc[2], Marie P. Cifuentes[1] and Mark G. Humphrey[1] (✉)

[1] *Research School of Chemistry, Australian National University, Canberra, ACT 2601, Australia.*
[2] *Faculty of Chemistry, Wroclaw University of Science and Technology, Wroclaw 50-370, Poland.*

Received: day month year / **Revised:** day month year / **Accepted:** day month year (automatically inserted by the publisher)

ABSTRACT

Oligo(*p*-phenyleneethynylene)s (OPEs) end-capped with (alkynyl)bis(diphosphine)ruthenium and thiol/thiolate groups stabilize ca. 2 nm diameter gold nanoparticles (AuNPs). The morphology, elemental composition and stability of the resultant organometallic OPE/AuNP hybrid materials have been defined using a combination of molecular- and nano-material chacterization techniques. The hybrids display long-term stability in solution (more than a month), good solubility in organic solvents, reversible ruthenium-centered oxidation, and transparency beyond 800 nm, and possess very strong nonlinear absorption activity at the first biological window, and unprecedented two-photon absorption activity in the second biological window (σ_2 up to 38,000 GM at 1050 nm).

KEYWORDS

Gold nanoparticles, inorganic materials, metal alkynyl complexes, nonlinear optics, organometallics

1 Introduction

Molecular and nano-materials that display nonlinear absorption (NLA) are attracting attention due to potential or demonstrated applications in optical data storage, imaging, optical limiting, telecommunications, medicine, and 3D-patterning [1-4]. Particular interest has been shown in tailoring materials with high transparency and efficient NLA activity in the near-infrared (NIR) spectral region, because NLA activity in this region will enable devices exploiting NLA to operate at technologically-important wavelengths such as the optical fiber windows (around 1300 and 1550 nm) and the second biological window (1000 – 1700 nm) [5]. A range of structural features of materials have been shown to advantageously impact on NLA performance [6-9]. For example, localized surface plasmon resonance (LSPR) at gold nanoparticles (AuNPs) can potentially afford strong NLA due to ultrafast field enhancement at the metal-dielectric interface [10]. Coating AuNPs with sulfur-containing species has afforded two-photon absorption (2PA) activity peaking in the visible and with weaker 2PA maxima extending into the NIR (to 800 nm) [11-14]. Despite these encouraging results, little is known of the wavelength-dependence of 2PA for AuNPs and their hybrids at longer wavelengths, the only report revealing modest 2PA for a captopril-AuNP hybrid (maximal cross-section σ_2 = 1510 GM @ 900 nm; 1 GM = 10^{-50} cm^4 s photon^{-1}; captopril = (2*S*)-1-[(2*S*)-2-methyl-3-sulfanylpropanoyl]pyrrolidine-2-carboxylic acid) [13].

Oligo(*p*-phenyleneethynylene)- (OPE-)based entities (rods, dendrimers, etc.) containing ruthenium alkynyl complex moieties exhibit strong 2PA and record multiphoton absorption (3PA and 4PA) cross-sections extending deep into the NIR [15, 16]. *trans*-[Ru(dppe)$_2$] (dppe = 1,2-bis(diphenylphosphino)ethane) is a key component of such efficient NLA-phores, because the dπ-pπ orbital overlap with alkynyl ligands gives rise to intense metal-to-ligand charge-transfer (MLCT) in the visible region, while it simultaneously confers high thermal stability and good solubility, crucial requirements for processability. Most OPE-functionalized AuNPs have employed thiol-terminated OPEs to afford self-assembled monolayers at gold and gold-thiolate molecular junctions [17], but organometallic examples are rare [18-20]. We herein describe the first AuNPs stabilized by OPE rods end-functionalized by ruthenium alkynyl units, and report that the resultant hybrids display long-term stability, good solubility, high transparency, very strong NLA at the first biological window, and unprecedented NLA in the second biological window.

2 Results and discussion

2.1 Syntheses

The new complexes *trans*-[Ru((C≡C-1,4-C$_6$H$_4$)$_n$C≡C-1,4-C$_6$H$_4$SCH$_2$CH$_2$SiMe$_3$)(C≡C-1,4-C$_6$H$_4$X)(dppe)$_2$] (n = 0, X = H (**1a**), NO$_2$ (**1b**); n = 1, X = H (**2a**),

Address correspondence to Mark G. Humphrey, mark.humphrey@anu.edu.au

NO_2 (**2b**); n = 2, X = H (**3a**), NO_2 (**3b**)) that were employed to construct the hybrids were prepared by extending published syntheses of *trans*-bis(alkynyl)bis(diphosphine)ruthenium complexes (Scheme S1-S2 in the electronic supplementary material (ESM)) [21-24]. All complexes were characterized by ^1H, ^{13}C and ^{31}P NMR spectroscopies, IR spectroscopy, mass spectrometry, and elemental analysis. The trimethylsilyl-protected thiol groups were positioned at the termini of the rod-like structures remote from the *trans*-[Ru(dppe)$_2$] fragment to minimize steric effects during AuNP stabilization. The organics 1,4-XC_6H_4C≡C-1,4-$C_6H_4SCH_2CH_2SiMe_3$ (X = H (**4a**), NO_2 (**4b**)) were prepared similarly (Scheme S3 in the ESM), to permit benchmarking of the influence of the *trans*-[Ru(dppe)$_2$] moiety on the physical and chemical properties of the hybrids and, ultimately, the NLA performance. The phenyl-terminated complexes **1a**, **2a**, and **3a** are soluble in common organic solvents, in contrast to the nitro end-functionalized analogues (**1b**, **2b**, and **3b**) which become increasingly less soluble in conventional organic solvents upon OPE bridge-lengthening. The ^{31}P NMR spectra of complexes **1a**, **2a**, and **3a** contain singlets at ca. 53.7 ppm (Figs. S7, S13, S19 in the ESM), while the spectra of complexes **1b**, **2b**, and **3b** display singlets in the range 53.1-53.3 ppm (Figs. S10, S16, S22 in the ESM), the singlets confirming *trans* configurations at the ruthenium center. The FT-IR spectra of all complexes contain a stretching vibration characteristic of the alkynyl fragment (C≡C) ligated to ruthenium in the range 2045-2058 cm^{-1}, consistent with the spectra of analogues [21, 24, 25]. A single-crystal X-ray diffraction study was undertaken on **1a**, confirming its composition (Figs. S40-S41 and Table S1 in the ESM).

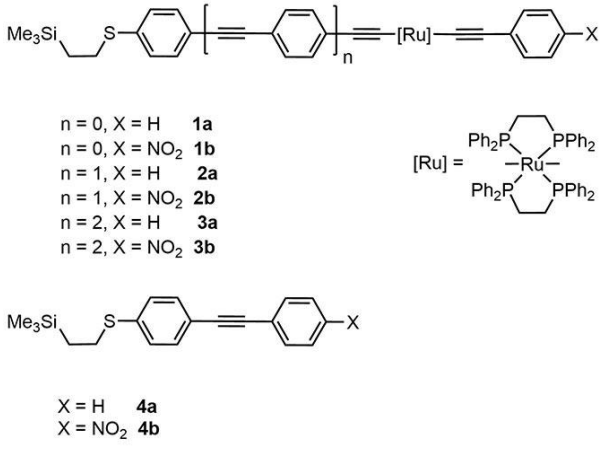

Figure 1. Compounds **1a-4b**.

The AuNP-hybrids were prepared by a modified Brust-Schiffrin method (Scheme 1) under strictly deoxygenated conditions [26, 27]. The thioether-containing organometallic and organic compounds were treated with tetra(*n*-butyl)ammonium fluoride to generate the thiolate species, which were then used without purification in the synthesis of the AuNP-hybrids. The resultant mixtures containing TMC/AuNP hybrids were poured into EtOH and placed in the refrigerator overnight to induce precipitation of the target materials and to remove the unreacted thiolate species. The TMC/AuNP hybrids were collected by filtration through a membrane and washed with EtOH and different fractions of petroleum spirits, affording dark purple solids in all cases (**1a-AuNP**, **2a-AuNP**, **2b-AuNP**, **3a-AuNP**, and **4a-AuNP**).

Other potential hybrids **1b-AuNP** and **4b-AuNP** could not be isolated because black precipitates formed shortly after the addition of the reducing agent (see for example, the ^1H and ^{31}P NMR of the unsuccesful AuNP synthesis employing **1b** (Figs. S38-S39)). It also proved impossible to obtain stable dispersions of **3b-AuNP** because it precipitated from conventional organic solvents, presumably due to the lack of solubility of complex **3b**. These three possible hybrids were therefore not pursued further.

The desilylation step is an essential part of the synthetic protocol; attempts to stabilize AuNPs without first deprotecting the corresponding 2-(trimethylsilyl)ethyl-protected thiol only afforded black insoluble precipitates. A sample of the resultant black insoluble material was suspended in DMF and supported on a transmission electron microscopy (TEM) grid by drop casting, the TEM study indicating that the material consists of amorphous aggregated gold particulate (Fig. S42 in the ESM). Thus, stabilization of AuNPs with such linear OPE-based molecules necessitates thiol/thiolate groups.

Scheme 1. Synthesis of hybrids **1a-AuNP**, **2a-AuNP**, **2b-AuNP**, **3a-AuNP**, and **4a-AuNP**. TMS = trimethylsilyl, TBAF = tetra(*n*-butyl)ammonium fluoride, TOAB = tetra(*n*-octyl)ammonium bromide.

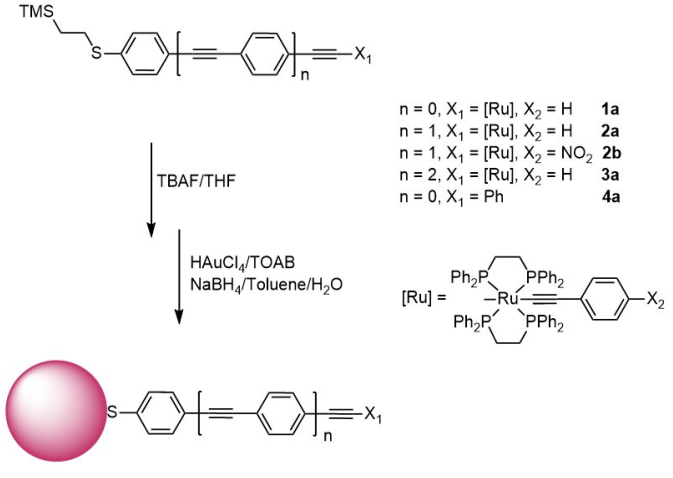

The synthesis of **2a-AuNP** was monitored by sampling the UV-Vis spectrum of the reaction mixture over a 24 h period, the results being used to inform the preparation of the other hybrids (**1a-AuNP**, **2b-AuNP**, **3a-AuNP**, and **4a-AuNP**). The UV-Vis studies suggested that complete passivation of the surface of the AuNPs was reached between 4 and 22 h of reaction, no further change in the UV-Vis spectrum being observed thereafter (Fig. 2a). The band at ca. 400 nm has a shoulder at 450 nm which is assumed to correspond to unreacted desilylated **2a**, because it is present in excess and it disappears following purification (Experimental Section, Fig. S43 in the ESM). The ^1H NMR spectra of the hybrids **1a-AuNP**, **2a-AuNP**, **2b-AuNP**, **3a-AuNP**, and **4a-AuNP** show the absence of resonances at ca. 3 and ca. 1 ppm, confirming removal of the $Me_3SiCH_2CH_2$- protecting groups on attachment of the ligands to the AuNPs (Figures 2b, S29, S31, S33, S35, S37 in the ESM). The ^{31}P NMR spectra of all hybrids display the characteristic singlet

of the *trans*-[Ru(dppe)$_2$] moiety at ca. 53 ppm, suggesting that the stabilizing organometallic units retain their integrity and do not decompose under the reaction conditions employed [11]. The stability of **2a-AuNP** was assessed in $CDCl_3$ solution by ^{1}H (Fig. S44 in the ESM) and ^{31}P (Fig. S45 in the ESM) NMR spectroscopies. The spectra of **2a-AuNP** were screened for 33 days and remained identical over this period. FT-IR studies in the far IR region contain broad absorption bands at ca. 250 cm^{-1} assigned to the characteristic vibrational modes of the Au-S bond [28], providing further evidence that compounds **1a**, **2a**, **2b**, **3a**, and **4a** have been successfully grafted onto the AuNP surface (Figs. S46-S55 in the ESM). For example, the far-IR spectrum of **2a-AuNP** contains a broad band at 258 cm^{-1} (spanning from ca. 180 cm^{-1} to ca. 320 cm^{-1}) while the same region of the spectrum of **2a** is almost featureless (Fig. 2c).

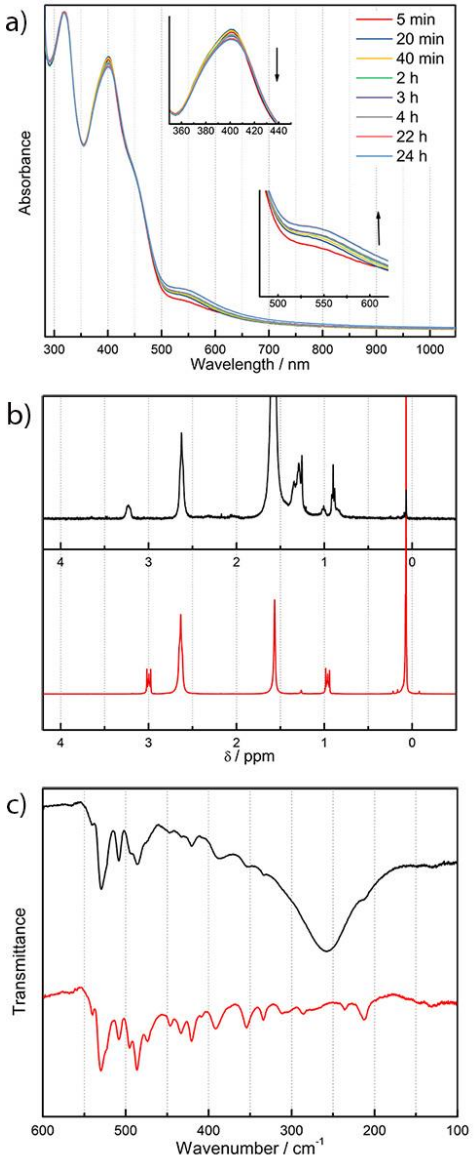

Figure 2. a) Time-dependent UV-Vis studies of the synthesis of **2a-AuNP** confirming reaction completion between 4 and 22 h; b) ^{1}H NMR spectra of **2a** and **2a-AuNP** in $CDCl_3$ confirming removal of the $Me_3SiCH_2CH_2$ group upon hybrid formation; and c) far IR spectra of **2a** (red) and **2a-AuNP** (black) confirming formation of Au-S linkages on hybrid formation.

2.2 Morphological and elemental studies of the hybrids

The morphology and composition of the hybrids **1a-AuNP**, **2a-AuNP**, **2b-AuNP**, **3a-AuNP**, and **4a-AuNP** were studied using TEM, dynamic light scattering (DLS), X-ray photoelectron spectroscopy (XPS), scanning electron microscopy-energy dispersive X-ray spectroscopy (SEM-EDX), and inductively coupled plasma-optical emission spectroscopy (ICP-OES), and the catalytic activity for reduction of 4-nitrophenol was assessed. The size of the cores and ligand shells of the new hybrids were estimated from TEM and DLS studies, the results being presented in Table 1. The TEM micrographs (Fig. 3, top) reveal that the hybrids have similar diameters (ca. 2 nm) and narrow size distributions (Fig. S56 in the ESM), and do not aggregate, due to the effective passivation of the AuNP surfaces by the stabilizing ligands in **1a-AuNP** (Fig. 3a, top), **2a-AuNP** (Fig. 3b, top), **2b-AuNP** (Fig. 3c, top), **3a-AuNP** (Fig. 3d, top), and **4a-AuNP** (Fig. 3e, top); in fact, self-assembly with homogeneous interparticle distances is suggested by the TEM images. The DLS results suggest that the AuNPs are stabilized by a monolayer of organometallic complexes (assuming lengths of the latter obtained from molecular modelling: Figs. S57-S59 in the ESM). All hybrids display low polydispersity indexes in THF, suggestive of high monodispersity of the colloids in solution (Table 1).

The elemental compositions of the hybrids were confirmed by qualitative XPS (Fig. 3, bottom). The sulfur results reveal more than one binding mode of the thiol functionality to the AuNP surface [29, 30]. For each hybrid, the XPS spectrum displays an S 2p peak at 162 eV. corresponding to the sulfur atom of the thiolate species on the AuNP surface [29]. Deconvolution of these peaks reveal more than one binding mode, suggesting coexistence of chemi- and physi-sorbed species on the AuNP surface (Fig. 3, bottom). The spectra of **2b-AuNP** (Fig. 3c, bottom) and **3a-AuNP** (Fig. 3d, bottom) contain peaks at ca. 168.5 eV and the spectrum of **4a-AuNP** (Fig. 3e, bottom) contains a peak at ca. 170.0 eV, all suggestive of the presence of oxidized sulfur species [31]. The high-resolution XPS spectra of Au, P, S, Ru, and C show binding energies for organoruthenium/AuNP hybrids consistent with literature data (Figs. S60-S64 in the ESM) [11]. The homogeneity of hybrids **1a-AuNP**, **2a-AuNP**, **2b-AuNP**, **3a-AuNP**, and **4a-AuNP** was confirmed by SEM-EDX in element mapping mode (Figs. S65-S69 in the ESM). ICP-OES of the ruthenium and gold content was employed to determine the number of organometallic OPE rods per AuNP, results being consistent with monolayer coverage [**1a-AuNP**: 52; **2a-AuNP**: 92; **2b-AuNP**: 58; **3a-AuNP**: 80; values ± 5 %], confirming results from DLS.

Table 1. Size distribution, hydrodynamic diameter, and polydispersity of **1a-AuNP**, **2a-AuNP**, **2b-AuNP**, **3a-AuNP**, and **4a-AuNP**.

Compound	Size distribution (nm)	Hydrodynamic diameter (nm)	Polydispersity index
1a-AuNP	2.5 ± 0.6	4.0 ± 0.7	0.02
2a-AuNP	2.3 ± 0.7	4.8 ± 0.4	0.01
2b-AuNP	1.8 ± 0.7	4.2 ± 0.6	0.02
3a-AuNP	2.3 ± 0.6	8.4 ± 1.6	0.04
4a-AuNP	2.2 ± 0.6	2.9 ± 0.4	0.02

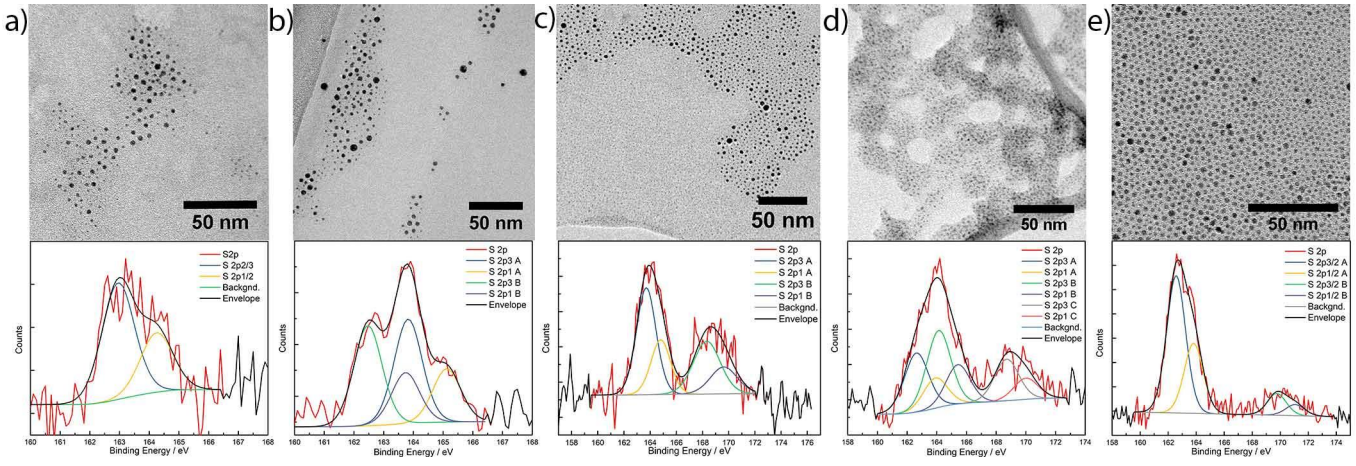

Figure 3. TEM micrograph (top) and high-resolution S 2p XPS spectra (bottom) for a) **1a-AuNP**, b) **2a-AuNP**, c) **2b-AuNP**, d) **3a-AuNP**, and e) **4a-AuNP**.

Catalysis occurs at the gold surface of the AuNPs, so assessing catalytic activity of the NPs can afford complementary information about the ease of access to gold sites, and therefore the coverage by the stabilizing groups. The catalytic activity for reduction of *p*-nitrophenol was assessed from the *p*-hydroxyaniline yield after 2 h. The yield of the organic hybrid **4a-AuNP** (61 %) is similar to **ndt-AuNP** (57 %) (ndt = *n*-dodecanethiol), while OPE π-system lengthening in the organometallic hybrids leads to an increase in catalytic activity proceeding from one (**1a-AuNP** (41 %)) to three (**3a-AuNP** (71 %)) PE units, consistent with the bulky ligated ruthenium centers being increasingly removed from the AuNP surface, and the AuNP surface gold atoms becoming increasingly accessible. The introduction of nitro substituent leads to a small reduction in activity (**2a-AuNP** (63 %) cf **2b-AuNP** (57 %)). It is tempting to ascribe this to a concomitant slight depletion of electron density at the AuNP surface, but the differences in activity are minor and, overall, the catalytic activity seems more closely correlated with steric considerations, as anticipated for a partial monolayer of a bulky stabilizing group.

2.3 Electrochemical studies

The cyclic voltammograms of the organometallic compounds exhibit one-electron quasi-reversible metal-centered oxidation events (Figs. S70-S75 in the ESM), in contrast to the reversible processes observed for analogous literature examples [32]. As expected, the phenyl-capped complexes **1a, 2a**, and **3a** are easier to oxidize than the nitro-capped complexes **1b**, **2b**, and **3b** (Table 2), and increasing the distance between the thiol and the metal center from one (**1a** $E_{1/2}$ $Ru^{II/III}$ = 0.47 V, **1b** $E_{1/2}$ $Ru^{II/III}$ = 0.58 V) to two (**2a** $E_{1/2}$ $Ru^{II/III}$ = 0.51 V, **2b** $E_{1/2}$ $Ru^{II/III}$ = 0.63 V) and then three (**3a** $E_{1/2}$ $Ru^{II/III}$ = 0.54 V, **3b** $E_{1/2}$ $Ru^{II/III}$ = 0.65 V) PE units shifts the oxidation event towards more positive potentials. This trend is consistent with a weakening of the electron-donating effect of the thiol on the *trans*-[Ru(dppe)$_2$] center as the distance between these groups is increased. The metal-centered oxidation events for **1-3** are quasi-reversible, likely due to the sulfur atom destabilizing the HOMO, and resulting in an electron-transfer process involving structural reorganization of the complex. The hybrids display similar oxidation potentials to the free organometallic complexes (Figs. S76-S79 in the ESM), with the exception of complex **1a** ($E_{1/2}$ $Ru^{II/III}$ = 0.56 V) for which a significant shift in potential is observed (Fig. S76 in the ESM).

Table 2. Linear optical absorption and cyclic voltammetry data for **1a**, **1b**, **2a**, **2b**, **3a, 3b**, **4a**, **4b**, **1a-AuNP**, **2a-AuNP**, **2b-AuNP**, **3a-AuNP**, and **4a-AuNP**.

Compound/Hybrid	λ_{max} (nm) [ε (10^4 M^{-1} cm^{-1})]			$E_{1/2}$ $Ru^{II/III}$ (V vs Ag/AgCl)	$i_{p,c}/i_{p,a}$	ΔE_p (V)
	THF	Toluene	DMF			
1a	340 [4.3]	340 [3.9]	341 [3.9]	0.47	0.92	0.15
1b	474 [3.2]	465 [2.4]	484 [2.4]	0.58	0.77	0.14
2a	391 [5.8]	390 [4.5]	392 [5.0]	0.51	0.84	0.12
2b	460 [3.2]	460 [2.7]	474 [2.9]	0.63	0.64	0.10
3a	415 [5.4]	410 [4.2]	413 [4.1]	0.54	0.85	0.11
3b	470 (sh) [3.6]	470 (sh) [3.2]	470 (sh) [3.0]	0.65	0.59	0.11
4a	308 [4.3]	315 [3.1]	310 [1.9]	N/A	N/A	N/A
4b	358 [2.8]	360 [2.4]	360 [1.6]	N/A	N/A	N/A
1a-AuNP	523 [LSPR]	524 [LSPR]	517 [LSPR]	0.53	0.88	0.17
2a-AuNP	526 [LSPR]	535 [LSPR]	532 [LSPR]	0.50	0.94	0.08
2b-AuNP	sh	sh	sh	0.63	0.79	0.10
3a-AuNP	sh	sh	sh	0.54	0.99	0.09
4a-AuNP	520 [LSPR]	530 [LSPR]	520 [LSPR]	N/A	N/A	

[a] Deconvolution was undertaken using OriginLab 2018 in peak analyzer mode [33].

The proximity of the ruthenium center to the AuNP surface in **1a-AuNP** has a strong electronic influence on its oxidation potential compared to its precursor **1a**, suggesting that the AuNP core is behaving as an electron-donating unit. The cathodic and anodic peaks of the ruthenium complex oxidation process become sharper and the peak-to-peak separations (ΔE_p) become smaller as the OPE bridge is lengthened and the distance between the thiol group and the metal center is increased [**1a** (ΔE_p = 0.15 V), **2a** (ΔE_p = 0.12 V), **3a** (ΔE_p = 0.11 V) and **1a-AuNP** (ΔE_p = 0.17 V), **2a-AuNP** (ΔE_p = 0.08 V), **3a-AuNP** (ΔE_p = 0.09 V)] (Table 2, Figs. S77-S79 in the ESM). The quasi-reversible electrochemical behavior suggests this new class of hybrids have potential in linear optical and nonlinear optical (NLO) switching [34].

2.4 Linear optical properties

The spectra of **1a-3b** display low-energy absorption bands assigned to the characteristic MLCT transitions of *trans*-Ru(dppe)$_2$ bis(alkynyl) complexes (Table 2) [21, 25, 35]. The MLCT bands of the examples with peripheral phenyl groups red-shift on moving from the complex with one PE group (**1a**, λ_{max} = 340 nm) to that with two (**2a**, λ_{max} = 391nm), and then three (**3a**, λ_{max} = 415 nm) (Fig. 4a). In the spectra of the complexes with peripheral nitrophenyl units **1b**, **2b**, and **3b**, the MLCT band is almost invariant at ca. 470 nm, shifting only slightly on π-bridge-lengthening (Fig. 4b) [25, 35]. These results indicate that the LUMOs of **1a**-**3a** are most likely localized on the OPE ligand, whereas the LUMOs of **1b**-**3b** are most likely localized at the 4-nitrophenylethynyl ligand, consistent with reports for analogues [21, 25, 35]. The UV-Vis spectra of the hybrids **1a-AuNP**, **2a-AuNP** and **4a-AuNP** show the characteristic LSPR bands, whereas the LSPR bands in the spectra of **3a-AuNP** and **3b-AuNP** are obscured by the low-energy MLCT bands of the metal alkynyl unit (Fig. 4c). These low-energy bands for **3a-AuNP** and **3b-AuNP** exhibit tails that extend to ca. 800 nm, in contrast to those of the organometallic OPE rod precursors (**3a** and **3b**), and consistent with underlying LSPR bands and thereby the presence of the AuNP cores. The LSPR bands of the hybrids red-shift when the OPE length is increased from one- (**1a-AuNP**) to two- (**2a-AuNP**) phenyleneethynylene units, with the largest difference in absorption maxima seen in DMF solvent ($\Delta\lambda_{max}$ = 15 nm). This red shift is consistent with that reported for the LSPR band in **ndt-AuNP** (5 nm diameter) following partial exchange of the ndt ligands by aryl thiols with an increasing number of benzene rings (thiophenol: λ_{LSPR} = 521 nm, 4-biphenylthiol: λ_{LSPR} = 528 nm, 4-terphenylthiol: λ_{LSPR} = 535 nm) [36]. The optical properties of the compounds and hybrids were studied in THF, toluene and DMF solvent to investigate the solvatochromic behavior of the complexes and hybrids (Table 2, Figs. S80-S85 in the ESM). The MLCT bands of the complexes exhibit weak positive solvatochromism while the LSPR bands of **1a-AuNP**, **2a-AuNP**, and **3b-AuNP** do not exhibit any appreciably solvatochromic behaviour in the solvents studied, consistent with effective passivation of the AuNP surface. Deconvolution of the spectra of all hybrids was performed to estimate the absorption maxima of the LSPR band when it was obscured by the MLCT band of the complexes in the hybrids (Figs. S86-S90 in the ESM), essential for hybrids **2b-AuNP** and **3a-AuNP**. We note that such deconvoluted maxima are suggested (in most cases) to be at higher energy than would be expected for LSPR bands.

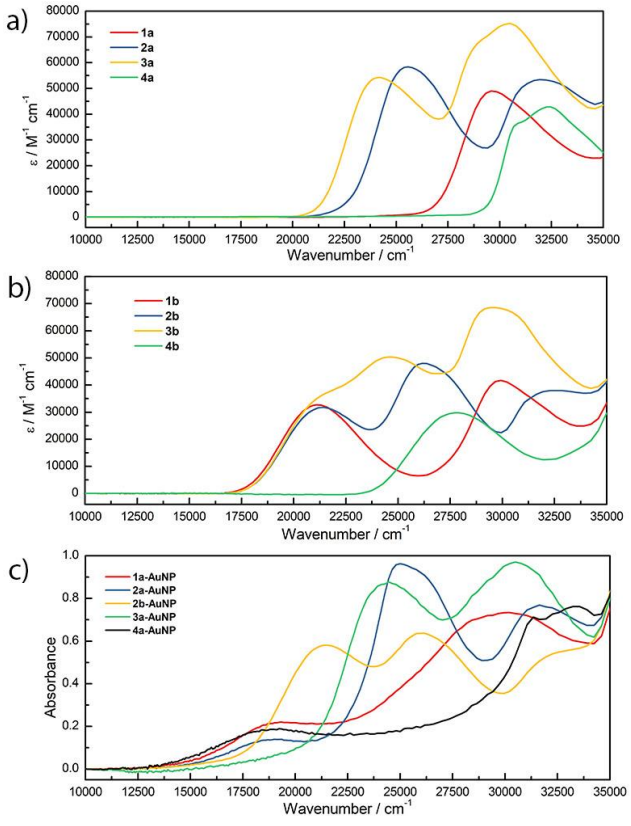

Figure 4. UV-Vis spectra of compounds **1a-4a** (a), **1b-4b** (b) and **1a-AuNP**, **2a-AuNP**, **2b-AuNP**, **3a-AuNP**, **4a-AuNP** (c).

2.5 Nonlinear optical properties

The third-order NLO properties of the organometallic and organic compounds and their AuNP hybrids were investigated using the Z-scan technique over the spectral range 540-1150 nm and employing an ultrashort pulse (130 fs) low repetition rate (1 kHz) laser to minimize contributions from excited-state absorption (ESA). The nonlinear refraction and NLA properties of the compounds were measured simultaneously using a combination of closed-aperture and open-aperture Z-scan, the resultant data being displayed in Figures S91-S116 in the ESM, and key NLA parameters being collected in Table 3. The molecular compounds **1-4** exhibit low to moderate $\sigma_{2,max}$ in the UV-Vis-NIR region, with values increasing upon metallation, increasing the length of the OPE bridge, and introduction of nitro group, consistent with data reported elsewhere;[21, 35] the wavelengths of the 2PA maxima blue shift upon nitration. The AuNP hybrids display saturable absorption (SA) in the shortest wavelength range explored (575–600 nm) (Table 3). Strong NLA behavior is observed at the low-energy end of the visible region (625–800 nm), but this is accompanied by substantial linear absorption, so significant contributions from ESA are anticipated, and we therefore use the term "effective" 2PA to account for the various contributions to NLA in this short wavelength region. With the exception of **1a-AuNP**, which

is NLA-inactive at wavelengths longer than 875 nm, the AuNP hybrids display exceptional 2PA at wavelengths extending well into the NIR region (800 – 1150 nm), with maximal values centered at ca. 1050 nm. This is despite the hybrids being transparent in the NIR region at wavelengths longer than 800 nm, and so consistent with minimal contributions from ESA and suggestive of a pure 2PA into the surface plasmon band. The σ_2 merit at 1050 nm increases markedly on organometallation (proceeding from **4a-AuNP** to **2a-AuNP**), and to a lesser extent on introduction of nitro group (proceeding from **2a-AuNP** to **2b-AuNP**) or ligand π-system lengthening (proceeding from **2a-AuNP** to **3a-AuNP**). The most efficient hybrid, **3a-AuNP**, displays exceptional activity in the second biological window ($\sigma_{2,1050}$ = 38,000 GM).

Table 3. Linear Optical and Nonlinear Optical Absorption Cross-Section Maxima for **1-4**, **1a-AuNP**, **2a-AuNP**, **2b-AuNP**, **3a-AuNP**, and **4a- AuNP**[a]

Compound or hybrid (FWt)[b]	1PA λ_{max} [ε]	σ_2 [λ_{max}, ε]	σ_2/FWt [λ_{max}][c]	Size distribution (nm)
1a (1232)	335 [4.9]	60 ± 10 [640, 0]	0.05 ± 0.01 [640]	-
1b (1277)	474 [0.8]	190 ± 20 [875, 0]	0.15 ± 0.02 [875]	-
2a (1332)	389 [7.4]	250 ± 20 [800, 0]	0.19 ± 0.01 [800]	-
2b (1377)	568 [2.6]	760 ± 50 [760, 0]	0.55 ± 0.04 [760]	-
3a (1432)	413 [5.1]	520 ± 90 [780, 0]	0.36 ± 0.06 [780]	-
3b (1477)	460 [2.5]	1580 ± 140 [800, 0]	1.07 ± 0.10 [800]	-
4a (310)	308 [4.3]	20 ± 8 [560, 0]	0.06 ± 0.01 [560]	-
4b (355)	360 [1.6]	74 ± 10 [560, 0]	0.21 ± 0.03 [560]	-
1a-AuNP (159,000 ± 38,000)	517 [2.5] (LSPR)	104,000 ± 18,000 [625, 16.0] 25,000 ± 4000 [800, 1.2]	0.65 ± 0.19 [625] 0.16 ± 0.05[800]	2.5 ± 0.6
2a-AuNP (205,000 ± 62,000)	526 [11.0] (LSPR)	172,000 ± 33,000 [650, 16.0] 190,000 ± 12,000 [775, 1.1] 38,000 ± 19,000 [875, 0] 20,000 ± 10,000 [1050, 0]	0.84 ± 0.30 [650] 0.93 ± 0.28 [775] 0.19 ± 0.11 [875] 0.10 ± 0.06 [1050]	2.3 ± 0.7
2b-AuNP (111,000 ± 43,000)	sh	170,000 ± 33,000 [625, 15.0] 123,000 ± 10,000 [775, 1.4] 52,000 ± 4000 [925, 0] 26,000 ± 4000 [1050, 0]	1.53 ± 0.67 [625] 1.11 ± 0.44 [775] 0.47 ± 0.19 [925] 0.23 ± 0.10 [1050]	1.8 ± 0.7
3a-AuNP (197,000 ± 51,000)	sh	232,000 ± 39,000 [600, 6.9] 116,000 ± 7000 [775, 0.1] 35,000 ± 5000 [925, 0] 38,000 ± 13000 [1050, 0]	1.18 ± 0.37 [600] 0.59 ± 0.16 [775] 0.18 ± 0.05 [925] 0.19 ± 0.08 [1050]	2.3 ± 0.6
4a-AuNP (65,000 ± 18000)	526 [9.8] (LSPR)	46,000 ± 3000 [675, 0.6] 26,000 ± 2000 [800, 0.4] 5500 ± 1500 [950, 0] 540 ± 130 [1050, 0]	0.71 ± 0.20 [675] 0.40 ± 0.11 [800] 0.08 ± 0.03 [950] 0.008 ± 0.003 [1050]	2.2 ± 0.6

[a] Measurements in THF solvent; λ_{max} in nm, [ε] in 10^4 M^{-1} cm^{-1}, σ_2 values in GM (1 GM = 10^{-50} cm^4 s); [b] FWt in grams per mole; the FWts of the hybrids **1a-AuNP**, **2a-AuNP**, **2b-AuNP** and **3a-AuNP** correspond to the sum of the average number of gold atoms per AuNP core (N_{Au}) and the average number of complexes ($N_{complex}$) in the hybrid (FWt = N_{Au} + $N_{complex}$). N_{Au} was estimated according to the following equation N_{Au} = $30.8960D^3$,[21] where D is the average AuNP diameter obtained from TEM analysis and $N_{complex}$ was estimated using N_{Au} as reference and determination of the Au:Ru ratio by ICP-OES analysis. For **4a-AuNP**, only N_{Au} was used to calculate the FWt, and the FWt-scaled data therefore represent an upper bound. [c] The error associated with the FWt was included in σ_2/FWt by using standard error propagation statistical analysis: $SD_{\sigma 2/FWt} = \sigma_2/FWt((CV_{\sigma 2})^2 + (CV_{FWt})^2)^{-1/2}$, where SD is the standard deviation and CV is the coefficient of variation. LSPR: localized surface plasmon resonance absorption maximum.

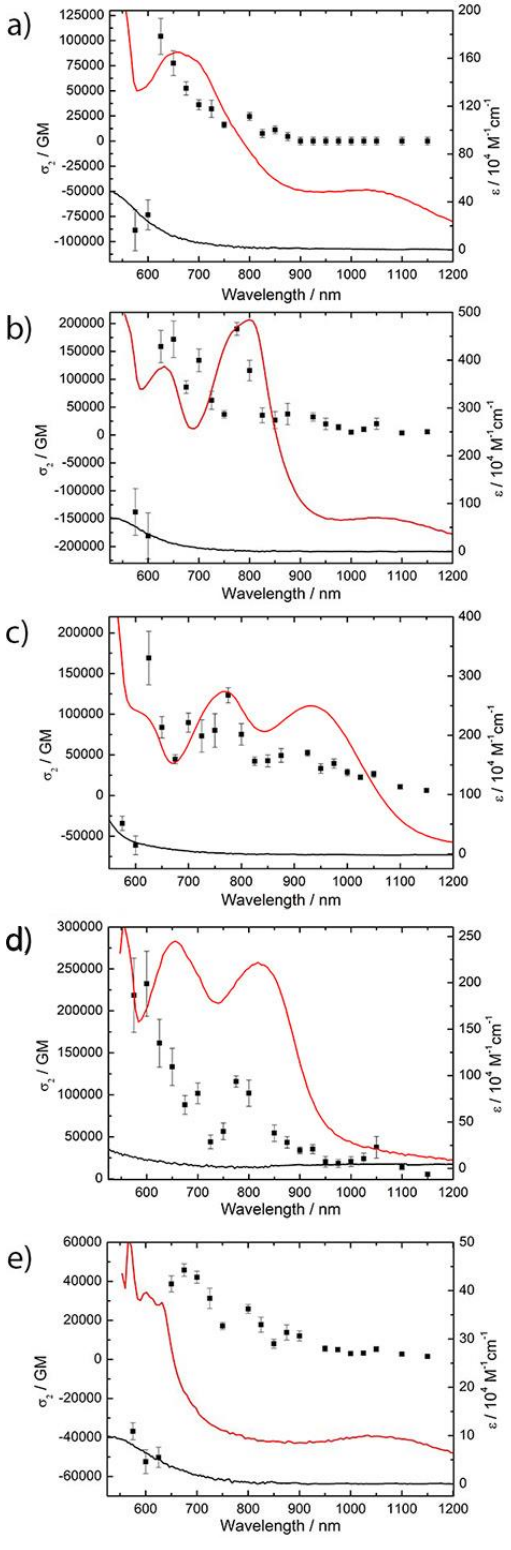

Figure 5. Plot of σ_2 overlaid on the UV-Vis spectrum (black), and including a plot of the UV-Vis as a function of twice (red) the wavelength for hybrids **1a-AuNP** (a), **2a-AuNP** (b), **2b-AuNP** (c), **3a-AuNP** (d), and **4a-AuNP** (e). 1 GM = 10^{-50} cm^4 s $photon^{-1}$.

Various methods have been employed to facilitate the comparison of σ_2 values of disparate materials, the σ_2/FWt merit figure being the most widely accepted [37, 38], but estimating the formula weights needed for such comparisons presents difficulties with nanoparticles and hybrids. In the present case, we have proceeded by estimating the FWts of the hybrids **1a-AuNP**, **2a-AuNP**, **2b-AuNP**, and **3a-AuNP** from the average number of gold atoms per AuNP core (N_{Au}) and the average number of complexes ($N_{complex}$) in the shell of the hybrid ($FWt = N_{Au} \times AtWt_{Au} + N_{complex} \times FWt_{complex}$), and ignoring the presence of any other species passivating the AuNPs. We assume the AuNP cores are pseudo-spherical in shape, and so $N_{Au} = 30.8960D^3$ [39], where D is the average AuNP diameter obtained from TEM, while $N_{complex}$ was estimated from the Au:Ru ratio determined by ICP-OES and using N_{Au} as reference. The resultant estimated FWts of the hybrids are provided in Table 3. Statistical analysis was employed to account for propagation of errors associated with the standard deviations of σ_2 and FWt (see footnote of Table 3), and thereby to avoid underestimation of these errors. Being mindful of the uncertainties that arise from this mathematical treatment, we then compared the weight-scaled NLA data for the hybrids (Table 3). Proceeding from the purely organic AuNP derivative **4a-AuNP** to the organoruthenium AuNP hybrids results in an enhancement of more than an order of magnitude in σ_2/FWt value at the same local NIR maximum, confirming the utility of an organometallic approach to AuNP passivation in the pursuit of NLA-efficient hybrids.

We have also explored the merit figure $\sigma_2/N_{complex}$, which has been suggested as a means of assessing if there is a nonlinear plasmonic enhancement in NLO properties upon loading chromophores onto AuNPs [40]. In contrast to the 5-(difluorenyl)-1,10-phenanthroline-based ruthenium complexes of this earlier study, for which results revealed an additive effect indicating no enhancement [40], the results from scaling σ_2 by $N_{complex}$ in the present work showed an outstanding 33-fold increase in the TPA performance of **1a-AuNP** (2000 ± 350 GM $complex^{-1}$ @ 625 nm) compared to the free complex **1a** (60 ± 10 GM $complex^{-1}$ @ 640 nm), while similarly nonlinear three-fold (**2b-AuNP**, **3a-AuNP**) and eight-fold (**2a-AuNP**) enhancement was observed for the other hybrids at wavelengths corresponding to the first biological window. We note that strong quenching of the emission quantum yield of the complexes is seen following attachment to the AuNPs (Figures S117-S123, Table S2 in the ESM), which we attribute to electron- or energy-transfer processes [41], and it is possible that this may contribute to increased local-field enhancement in the excited states of the organometallic-AuNP hybrids and thereby enhanced 2PA activity in the NIR.

3 Conclusion

We have described the first examples of AuNPs stabilized by OPE rods that are end-functionalized by alkynylruthenium units. These hybrids exhibit a range of useful properties (long-term stability, good solubility, high transparency, redox activity, and very strong NLA activity at the first biological window) and, where comparisons are possible, have been shown to display superior performance to purely organic OPE rod/AuNP hybrid analogues and a nonlinear plasmonic enhancement in NLA in the red/NIR region. The new organometallic AuNP hybrids from the present study have been shown to exhibit unprecedented NLA activity in the second biological window and are therefore of potential applications interest. These studies emphasize the advantage of an organometallation approach in the design of

efficient NLA materials.

Acknowledgements

We thank the Australian Research Council (DP170100411: M.G.H. and M.S.) and the National Science Centre (NCN) Poland (UMO-2016/22/M/ST4/00275: J.K.Z. and M.S.) for support of this work. C.Q. thanks Becas Chile (Agencia Nacional de Investigación y Desarrollo) for financial support in the form of a PhD scholarship (2015-72160061), J.P.L.M. thanks the Australian Government for an Australian Postgraduate Award, J.D. thanks the China Scholarship Council and the Australian National University for a CSC-ANU scholarship, and J.K.Z. thanks the Foundation for Polish Science (FNP) for support. The authors acknowledge the facilities, and the scientific and technical assistance, of the Australian Microscopy & Microanalysis Research Facility and the Centre of Advanced Microscopy at the Australian National University.

Electronic Supplementary Material: Supplementary material with details on experimental materials, instrumentation, procedures, X-ray structure determinations, NMR and UV–vis spectra, cyclic voltammetry and stability studies, nanoparticle size distribution histograms, X-ray spectroscopy, crystallography, catalytic studies, molecular modeling, Z-scan studies, and fluorescence studies is available in the online version of this article at http://dx.doi.org/10.1007/s12274-***-****-* (automatically inserted by the publisher).

References

[1] Tutt, A. L. W.; Boggess, T. F. A review of optical limiting mechanisms and devices using organics, fullerenes, semiconductors and other materials. *Progr. Quant. Electr.* **1993**, *17*, 299–338.

[2] Kim, B. H. M.; Cho, B. R. Small-molecule two-photon probes for bioimaging applications. *Chem. Rev.* **2015**, *115*, 5014–5055.

[3] Chen, C. G.; Roy, I.; Yang, C.; Prasad, P. N. Nanochemistry and nanomedicine for nanoparticle-based diagnostics and therapy. *Chem. Rev.* **2016**, *116*, 2826–2885.

[4] Dini, D. D.; Calvete, M. J. F.; Hanack, M. Nonlinear optical materials for the smart filtering of optical radiation. *Chem. Rev.* **2016**, *116*, 13043–13233.

[5] Smith, A. M.; Mancini, M. C.; Nie, S. Second window for *in vivo* imaging. *Nat. Nanotech.* **2009**, *4*, 710–711.

[6] He, G. S.; Tan, L. S.; Zheng, Q.; Prasad, P. N. Multiphoton absorbing materials: molecular designs, characterizations, and applications. *Chem. Rev.* **2008**, *108*, 1245–1330.

[7] Samoc, M.; Dalton, G. T.; Gladysz, J. A.; Zheng, Q.; Velkov, Y.; Agren, H.; Norman, P.; Humphrey, M. G. Cubic nonlinear optical properties of platinum-terminated polyynediyl chains. *Inorg. Chem.* **2008**, *47*, 9946–9957.

[8] Roberts, R. L.; Schwich, T.; Corkery, T. C.; Cifuentes, M. P.; Green, K. A.; Farmer, J. D.; Low, P. J.; Marder, T. B.; Samoc, M.; Humphrey, M. G. Organometallic complexes for nonlinear optics. 45. Dispersion of the third-order nonlinear optical properties of triphenylamine-cored alkynylruthenium dendrimers. *Adv. Mater.* **2009**, *21*, 2318–2322.

[9] Zhou, G. J.; Wong, W. Y. Organometallic acetylides of Pt^{II}, Au^{I} and Hg^{II} as new generation optical power limiting materials. *Chem. Soc. Rev*. **2011**, *40*, 2541-2566.

[10] Kamat, P. V. Photophysical, photochemical and photocatalytic aspects of metal nanoparticles. *J. Phys. Chem. B* **2002**, *106*, 7729−7744.

[11] Quintana, C.; Morshedi, M.; Wang, H.; Du, J.; Cifuentes, M. P.; Humphrey, M. G. Exceptional two-photon absorption in alkynylruthenium–gold nanoparticle hybrids. *Nano Lett.* **2019**, *19*, 756−760.

[12] Ramakrishna, G.; Varnavski, O.; Kim, J.; Lee, D.; Goodson, T. Quantum-sized gold clusters as efficient two-photon absorbers. *J. Am. Chem. Soc*. **2008**, *130*, 5032−5033.

[13] Olesiak-Banska, J.; Waszkielewicz, M.; Matczyszyn, K.; Samoc, M. A closer look at two-photon absorption, absorption saturation and nonlinear refraction in gold nanoclusters. *RSC Adv.* **2016**, *6*, 98748–98752.

[14] Olesiak-Banska, J.; Waszkielewicz, M.; Obstarczyka, P.; Samoc, M. Two-photon absorption and photoluminescence of colloidal gold nanoparticles and nanoclusters. *Chem. Soc. Rev.* **2019**, *48*, 4087–4117.

[15] Simpson, P. V.; Watson, L. A.; Barlow, A.; Wang, G.; Cifuentes, M. P.; Humphrey, M. G. Record multiphoton absorption cross-sections by dendrimer organometalation. *Angew. Chem. Int. Ed.* **2016**, *55*, 2387–2391.

[16] Schwich, T.; Barlow, A.; Cifuentes, M. P.; Szeremeta, J.; Samoc, M.; Humphrey, M. G. Stellar multi-photon absorption materials: beyond the telecommunication wavelength band. *Chem. Eur. J.* **2017**, *23*, 8395–8399.

[17] Stapleton, J. J.; Harder, P.; Daniel, T. A.; Reinard, M. D.; Yao, Y.; Price, D. W.; Tour, J. M.; Allara, D. L. High-resolution X-ray photoelectron spectra of organosulfur monolayers on Au(111): S(2p) spectral dependence on molecular species. *Langmuir* **2003**, *19*, 8245–8255.

[18] Al-Owaedi, O. A.; Milan, D. C.; Oerthel, M.-C.; Bock, S.; Yufit, D. S.; Howard, J. A. K.; Higgins, S. J.; Nichols, R. J.; Lambert, C. J.; Bryce, M. R.; Low, P. J. Experimental and computational studies of the single-molecule conductance of Ru(II) and Pt(II) *trans*-bis(acetylide) complexes. *Organometallics* **2016**, *35*, 2944–2954.

[19] Ng, Z.; Loh, K. P.; Li, L.; Ho, P.; Bai, P.; Yip, J. H. Synthesis and electrical characterization of oligo(phenylene ethynylene) molecular wires coordinated to transition metal complexes. *ACS Nano* **2009**, *3*, 2103–2114.

[20] Quintana, C.; Cifuentes, M. P.; Humphrey, M. G. Transition metal complex/gold nanoparticle hybrid materials. *Chem. Soc. Rev.* **2020**, *49*, 2316-2341.

[21] Hurst, S. K.; Cifuentes, M. P.; Morrall, J. P. L.; Lucas, N. T.; Whittall, I. R.; Humphrey, M. G.; Asselberghs, I.; Persoons, A.; Samoc, M.; Luther-Davies, B.; Willis, A. C. Organometallic complexes for nonlinear optics. 22. Quadratic and cubic hyperpolarizabilities of *trans*-bis(bidentate phosphine)ruthenium σ-arylvinylidene and σ-arylalkynyl complexes. *Organometallics* **2001**, *20*, 4664–4675.

[22] Touchard, D.; Morice, C.; Cadierno, V.; Haquette, P.; Toupet, L.; Dixneuf, P. H. Novel allenylidene alkynyl and ammonia alkynyl metal complexes via selective synthesis of mono and bis alkynyl ruthenium(II) complexes; crystal structure of *trans*-$[Ru(NH_3)(C{\equiv}CPh)(Ph_2PCH_2CH_2PPh_2)_2]PF_6$. *J. Chem. Soc. Chem. Commun.* **1994**, 859–860

[23] Touchard, D.; Haquette, P.; Guesmi, S.; Le Pichon, L.; Daridor, A.; Toupet, L.; Dixneuf, P. H. Vinylidene-, alkynyl-, and *trans*-bis(alkynyl)ruthenium complexes. Crystal structure of *trans*-$[Ru(NH_3)(C{\equiv}CPh)(Ph_2PCH_2CH_2PPh_2)_2]PF_6$. *Organometallics* **1997**, *16*, 3640–3648.

[24] McDonagh, A. M.; Whittall, I. R.; Humphrey, M. G.; Hockless, D. C. R.; Skelton, B. W.; White, A. H. Organometallic complexes for nonlinear optics VI: syntheses of rigid-rod ruthenium σ-acetylide complexes bearing strong acceptor ligands; X-ray crystal structures of trans-$[Ru(C{\equiv}CC_6H_4NO_2\text{-}4)_2(dppm)_2]$ and *trans*-$[RuC{\equiv}CC_6H_4C_6H_4NO_2\text{-}4,4')_2(dppm)_2]$. *J. Organomet. Chem.* **1996**, *523*, 33–40.

[25] Babgi, B. A.; Kodikara, M. S.; Morshedi, M.; Wang, H.; Quintana, C.; Schwich, T.; Moxey, G. J.; Van Steerteghem, N.; Clays K.; Stranger, R.; Cifuentes, M. P.; Humphrey, M. G. Linear optical, quadratic and cubic nonlinear optical, electrochemical, and theoretical studies of "rigid-rod" bis-alkynyl ruthenium complexes. *ChemPlusChem* **2018**, *83*, 630–632.

[26] Brust, M.; Walker, M.; Bethell, D.; Schiffrin, D. J.; Whyman, R. Synthesis of thiol-derivatised gold nanoparticles in a two–phase liquid–liquid system. *J. Chem. Soc. Chem. Commun.* **1994**, 801–802.

[27] Zhai, L.; McCullough, R. D. *J. Mater. Chem.* **2004**, *14*, 141–143.

[28] Bürgi, T. Properties of the gold–sulphur interface: from self-assembled monolayers to clusters. *Nanoscale* **2015**, *7*, 15553–15567.

[29] Pensa, E.; Cortés, E.; Corthey, G.; Carro, P.; Vericat, C.; Fonticelli, M. H.; Benítez, G.; Rubert, A. A.; Salvarezza, R. C. The chemistry of the

sulfur-gold interface: in search of a unified model. *Acc. Chem. Res.* **2012**, *45*, 1183–1192.

[30] Castner, D. X-ray photoelectron spectroscopy sulfur 2p study of organic thiol and disulfide binding interactions with gold surfaces. *Langmuir* **1996**, *12*, 5083–5086.

[31] Qie, L.; Chen, W.; Xiong, X.; Hu, C.; Zou, F.; Hu, P.; Huang, Y. Sulfur-doped carbon with enlarged interlayer distance as a high-performance anode material for sodium-ion batteries. *Adv. Sci.* **2015**, *2*, 1500195–1500201.

[32] Mulas, A.; Hervault, Y-M.; He, X.; Di Piazza, E.; Norel, L.; Rigaut, S.; Lagrost, C. Fast electron transfer exchange at self-assembled monolayers of organometallic ruthenium(II) σ-arylacetylide complexes. *Langmuir* **2015**, *31*, 7138-7147.

[33] OriginPro, Version 2018. OriginLab Corporation, Northampton, MA, USA.

[34] Green, K. A.; Cifuentes, M. P.; Corkery, T. C.; Samoc, M.; Humphrey, M. G. Switching the cubic nonlinear optical properties of an electro-, halo-, and photochromic ruthenium alkynyl complex across six states. *Angew. Chem. Int. Ed.* **2009**, *48*, 7867–7870.

[35] Babgi, B.; Rigamonti, L.; Cifuentes, M. P.; Corkery, T. C.; Randles, M. D.; Schwich, T.; Petrie, S.; Stranger, R.; Teshome, A.; Asselberghs, I.; Clays, K.; Samoc, M.; Humphrey, M. G. Length-dependent convergence and saturation behavior of electrochemical, linear optical, quadratic nonlinear optical, and cubic nonlinear optical properties of dipolar alkynylruthenium complexes with oligo(phenyleneethynylene) bridges. *J. Am. Chem. Soc.* **2009**, *131*, 10293-10307.

[36] Goldmann, C.; Lazzari R.; Paquez, X.; Boissière, C.; Ribot, F.; Sanchez, C.; Chanéac C.; Portehault, D. Charge transfer at hybrid interfaces: plasmonics of aromatic thiol-capped gold nanoparticles. *ACS Nano* **2015**, *9*, 7572-7582.

[37] Perez-Moreno, J.; Kuzyk, M. G. Comment on "Organometallic complexes for nonlinear optics. 45. Dispersion of the third-order nonlinear optical properties of triphenylamine-cored alkynylruthenium dendrimers" - Increasing the nonlinear optical response by two orders of magnitude. *Adv. Mater.* **2011**, *23*, 1428–1432.

[38] Schwich, T.; Cifuentes, M. P.; Gugger, P. A.; Samoc, M.; Humphrey, M. G. Electronic, molecular weight, molecular volume, and financial cost - scaling and comparison of two-photon absorption efficiency in disparate molecules (Organometallic complexes for nonlinear optics. 48.) - A response to "Comment on 'Organometallic complexes for nonlinear optics. 45. Dispersion of the third-order nonlinear optical properties of triphenylamine-cored alkynylruthenium dendrimers.' Increasing the nonlinear response by two orders of magnitude." *Adv. Mater.* **2011**, *23*, 1433–1435.

[39] Liu, X.; Atwater, M.; Wang, J.; Huo, Q. Extinction coefficient of gold nanoparticles with different sizes and different capping ligands. *Colloids Surf. B, Biointerfaces* **2007**, *58*, 3–7.

[40] Moreau, J.; Lux, F.; Four, M.; Olesiak-Banska, J.; Matczyszyn, K.; Perriat, P.; Frochot, C.; Arnoux, P.; Tillement, O.; Samoc, M.; Ponterini, G.; Roux, S.; Lemercier G. A 5-(difluorenyl)-1,10-phenanthroline-based Ru(II) complex as a coating agent for potential multifunctional gold nanoparticles. *Phys. Chem. Chem. Phys.* **2014**, *16*, 14826–14833.

[41] Zhang, T.; Zhao, T,; Yuan, P.; Xu, Q.-H. Surface Plasmon Enhanced, Coupled and Controlled Fluorescence. Geddes, C. D.; Ed.; Wiley, Hoboken: New Jersey, 2017, pp 211–225.

TSINGHUA UNIVERSITY PRESS Springer